Sustainable Energy & Fuels

ROYAL SOCIETY OF CHEMISTRY

PAPER

Cite this: *Sustainable Energy Fuels*, 2020, **4**, 6085

Polymeric carbon nitride coupled with a molecular thiomolybdate catalyst: exciton and charge dynamics in light-driven hydrogen evolution†

Ashwene Rajagopal,[a] Elham Akbarzadeh,[aj] Chunyu Li,[bc] Dariusz Mitoraj,[d] Igor Krivtsov,*[d] Christiane Adler,[d] Thomas Diemant,[e] Johannes Biskupek,[f] Ute Kaiser,[f] Changbin Im,[d] Magdalena Heiland,[a] Timo Jacob,[dgh] Carsten Streb,*[agh] Benjamin Dietzek*[bci] and Radim Beranek*[d]

Solar hydrogen evolution from water is a necessary step to overcome the challenges of rising energy demand and associated environmental concerns. Low-cost photocatalytic architectures based on polymeric light absorbers coupled to highly efficient molecular catalysts might represent an attractive platform to address this issue. However, to-date, our mechanistic knowledge of these systems is still largely underdeveloped. In this study, a molecular molybdenum sulfide hydrogen evolving catalyst, $[Mo_3S_{13}]^{2-}$, is loaded onto polymeric carbon nitride (CN_x) photoabsorber by impregnation. The resulting composite shows enhanced photocatalytic activity for hydrogen evolution compared to pristine CN_x under monochromatic visible light ($\lambda = 420$ nm) irradiation in the presence of sacrificial reducing agents. The light-driven dynamics of excitons and charges involved in hydrogen evolution catalysis were studied by a combination of spectroscopic (steady-state and time-resolved photoluminescence, femtosecond time-resolved transient absorption) and photoelectrochemical (open-circuit photopotential transients) methods. We demonstrate that the molecular molybdenum sulfide catalyst, at optimum loading (10 wt% nominal), improves the charge separation in the CN_x absorber by facilitating the depopulation of emissive (band-edge) or non-emissive (shallow trap) states, followed by an effectively catalyzed transfer of electrons from the charge-separated state (deep trap) to protons in the solution. The results provide important insights into the complex interplay between polymeric light absorbers and molecular redox catalysts, indicating that the electron transfer to the catalyst occurs on relatively longer (nanosecond to seconds) time scale, as the catalyst had no impact on the ultrafast (sub-nanosecond) photoinduced kinetics in the CN_x. These findings are of crucial importance for further development of soft-matter based architectures for solar fuels production.

Received 11th September 2020
Accepted 12th October 2020

DOI: 10.1039/d0se01366h

rsc.li/sustainable-energy

1. Introduction

Sunlight-driven photocatalytic hydrogen evolution reaction (HER) remains one of the greatest challenges on the way towards sustainable alternatives to fossil fuels.[1] A vast range of materials and approaches intended to tackle this goal have been investigated, and the pertinent research results have now been summarized in numerous review papers.[2–5] The challenge is far from trivial: in order to be implemented in real life, the photocatalyst must be highly active, selective and stable, and at the same time based on low-cost and abundant elements. Hence, there is a quest for replacing conventional, mostly metal oxide-based semiconductors and noble metal co-catalysts with more affordable alternatives.[6] In 2009, X. Wang *et al.* stirred the

[a]*Institute of Inorganic Chemistry I, Ulm University, Albert-Einstein-Allee 11, 89081 Ulm, Germany. E-mail: carsten.streb@uni-ulm.de*

[b]*Institute of Physical Chemistry, Abbe Center of Photonics, Friedrich Schiller University Jena, Lessingstr. 10, 07743 Jena, Germany. E-mail: benjamin.dietzek@uni-jena.de*

[c]*Department Functional Interfaces, Leibniz Institute of Photonic Technology (IPHT), Albert-Einstein-Str. 9, 07745 Jena, Germany*

[d]*Institute of Electrochemistry, Ulm University, Albert-Einstein-Allee 47, 89081 Ulm, Germany. E-mail: igor.krivtsov@uni-ulm.de; radim.beranek@uni-ulm.de*

[e]*Institute of Surface Chemistry and Catalysis, Ulm University, Albert-Einstein-Allee 47, 89081 Ulm, Germany*

[f]*Electron Microscopy of Materials Science, Central Facility for Electron Microscopy, Ulm University, Albert-Einstein-Allee 11, 89081, Ulm, Germany*

[g]*Helmholtz Institute Ulm (HIU), Helmholtzstr. 11, 89081, Ulm, Germany*

[h]*Karlsruhe Institute of Technology (KIT), P.O. Box 3640, 76021, Karlsruhe, Germany*

[i]*Center for Energy and Environmental Chemistry Jena (CEEC Jena), Philosophenweg 7a, 07743 Jena, Germany*

[j]*Department of Chemistry, Sharif University of Technology, Tehran, Iran*

† Electronic supplementary information (ESI) available. See DOI: 10.1039/d0se01366h

research community with the discovery of photocatalytic properties of polymeric carbon nitride (also referred in literature as melon, CN_x, C_3N_4 polymer, or g-C_3N_4).[7] This finding gave rise to a large number of publications on carbon nitride polymers modified with various co-catalysts, such as Pt and other noble metals,[8–10] metal–organic complexes,[11] metal phosphides,[12] metal borides,[13] and metal sulphides.[14] The latter received a special attention as WS_2 (ref. 15) or MoS_2 (ref. 16) were demonstrated to be efficient alternatives to the benchmark Pt catalysts for HER. However, in such layered metal sulfides only the undercoordinated edge sulfur atoms act as active sites for hydrogen evolution, while the rest of their 2D structure is inert.[17] This finding prompted the search for molecular[18] or nanoparticulate forms[19] of these materials, with the aim to maximize the number of exposed active species. The $[Mo_3S_{13}]^{2-}$ molecular clusters have been established as one of such promising co-catalysts for dark electrocatalytic[17,20–23] and photocatalytic HER under heterogeneous[24–26] and homogeneous conditions.[27,28] Anchoring of the cluster onto various solid catalyst supports or light absorbers is straightforward and has been demonstrated for TiO_2,[29] carbon materials,[21,22] and recently also for polymeric carbon nitride-based material.[26] More specifically, X. Wang *et al.* have coupled $[Mo_3S_{13}]^{2-}$ [= $\{Mo_3\}$] to protonated mesoporous carbon nitride with rod-like morphology (diameter *ca.* 1 μm), and the activity in photocatalytic HER of the hybrid was reported to be comparable with that of Pt-modified mesoporous carbon nitride using lactic acid as sacrificial electron donor.[26] However, to the best of our knowledge, no insight into the interaction and charge transfer processes between the support and co-catalyst has been presented so far. Herein, we demonstrate that $\{Mo_3\}$ deposited onto conventional polymeric carbon nitride can effectively catalyse visible light-driven hydrogen evolution using methanol as a reducing agent. Furthermore, using a combination of spectroscopic (steady-state and time-resolved photoluminescence, transient absorption) and photoelectrochemical (open-circuit photopotential) tools we shed light on the complex interplay between the carbon nitride light absorber and the molecular $\{Mo_3\}$ catalyst influencing the exciton dynamics and the kinetics of catalytic turnover in light-driven hydrogen evolution.

2. Experimental

2.1 Materials

Melamine, hexachloroplatinic acid hydrate ($H_2PtCl_6 \cdot nH_2O$), triethanolamine (TEOA) were purchased from Aldrich, methanol was supplied by VWR chemicals. $(NH_4)_6[Mo_7O_{24}] \cdot 4H_2O$ and methanol for catalysis was purchased from Aldrich. Ammonium polysulfide was purchased from Chemos GmbH.

2.2 Synthesis

Synthesis of polymeric carbon nitride. The polymeric carbon nitride (CN_x) was prepared by thermal polycondensation of 30 g melamine at 530 °C for 4 h in a lid-covered crucible.

Synthesis of $(NH_4)_2[Mo_3S_{13}] \cdot 2H_2O$. The thiomolybdate $(NH_4)_2[Mo_3S_{13}] \cdot 2H_2O$ was prepared by a modification of the synthesis reported by Müller *et al.*[30] $(NH_4)_6[Mo_7O_{24}] \cdot 4H_2O$ (4.0 g, 3.2 mmol) was dissolved in water (20 mL) in a round bottom flask, then ammonium polysulfide ($(NH_4)_2S_x$) solution (120 mL, 25 wt%) was added to it and fitted with condenser. The solution was heated to 96 °C for five days with slow stirring. Dark-red crystals of $(NH_4)_2[Mo_3S_{13}] \cdot 2H_2O$ formed and were removed by filtration, washed with water, ethanol, carbon disulfide and ether. Finally, the product was air-dried. Yield: 5.6 g (7.16 mmol, 97.9% based on Mo).

Synthesis of $Na_2[Mo_3S_{13}] \cdot 5H_2O$. $Na_2[Mo_3S_{13}] \cdot 5H_2O$ was synthesized as follows. $(NH_4)_2[Mo_3S_{13}] \cdot 2H_2O$ (3.02 g, 3.86 mmol) was suspended in an aqueous NaOH solution (1 wt%, 40 mL) and stirred under reduced pressure (20 mbar) for 2 h, in order to remove ammonium as NH_3 gas. The resulting dark red solution was filtered into an aqueous NaCl solution (10 wt%, 100 mL). After 12 h, the precipitated product was isolated by filtration, washed with 2-propanol and diethyl ether, and dried *in vacuo* at room temperature to give red-brown powder of $Na_2[Mo_3S_{13}] \cdot 5H_2O$. Yield: 3.20 g (3.78 mmol, 95.9% based on Mo).

Synthesis of CN_x–$\{Mo_3\}$ composites. CN_x–$\{Mo_3\}$ hybrids were synthesized through a two-step deposition process at room temperature. In a typical procedure, 20 mg of as-prepared CN_x was dispersed in 20 mL of methanol by ultrasonication for 3 h to prepare a homogenous suspension. Then, a measured amount of $Na_2[Mo_3S_{13}]$ (soluble in methanol) was added to it and stirred for 24 h. The solid was collected by centrifugation and three times washed with methanol to remove the excess of $\{Mo_3\}$. Finally, the obtained precipitates were air-dried at room temperature under ambient conditions giving CN_x–$\{Mo_3\}$. Different loadings of $\{Mo_3\}$ were deposited onto the CN_x material.

Synthesis of Pt-modified CN_x. The platinized CN_x (CN_x–Pt) was prepared as a benchmark photocatalyst using a photodeposition method. For this, the CN_x powder (0.2 g) was suspended in 20 mL H_2O : MeOH (9 : 1, v/v) solution containing hexachloroplatinic acid (4 mg), ultrasonicated for 1 h, bubbled with argon gas and irradiated for 30 min with a 150 W Xe-lamp equipped with a KG3 (Schott) heat filter. Subsequently, the powder was washed by centrifugation and dried overnight at 60 °C.

2.3 Characterization

ICP-AES. The actual loading of molybdenum sulfide cluster in the samples was determined using an inductively coupled plasma atomic emission spectrometer (ICP-AES, Horiba Jobin Yvon). For this, the Mo–CN_x–$\{Mo_3\}$ samples were dissolved in 1 M KOH at 100 °C in autoclave.

FT-IR spectroscopy. FT-IR spectroscopy was performed on a Shimadzu FT-IR-8400S spectrometer. Samples were prepared as KBr pellets.

X-ray powder diffraction (XRD). XRD was collected on a Rigaku XRD-6000 diffractometer using Cu Kα radiation (λ = 0.154 nm).

Thermogravimetric analysis (TGA). TGA was performed on a Setaram Setsys CS Evo (30–1000 °C at 10 K min^{-1}, 50 mL min^{-1} air, Graphite crucible 0.5 mL).

X-ray photoelectron spectroscopy (XPS). XPS measurements were performed with a PHI 5800 MultiTechnique ESCA system using monochromatized Al Kα radiation (250 W, 15 kV) and pass energies of 93.9 and 29.35 eV for survey and detail spectra, respectively, at a detection angle of 45°. The measurements were analyzed with the CasaXPS software, using a Shirley-type background and peaks of Gaussian–Lorentzian peak shape (70% G/30% L).

Transmission electron microscopy (TEM). The samples were dispersed in ethanol (supersonic bath) and drop-cast on holey carbon TEM grids. The TEM investigations were carried out using an image-side corrected FEI Titan 80-300 microscope operating at 80 kV. Imaging included diffraction pattern from selected areas and high resolution (HR) TEM. Energy filtered imaging exploiting absorption edges for elemental mapping were acquired using a Gatan GIF Quantum energy filter attached to microscope.

Diffuse reflectance spectroscopy (DRS). Diffuse reflectance UV-vis spectra of solids were recorded using a Shimadzu UV2600 UV-vis spectrophotometer from the samples pressed in pellets with $BaSO_4$.

Spectroscopic characterization. Polymeric carbon nitride suspensions for spectroscopic study were prepared by sonicating the carbon nitrides in deionized water (2 mg mL^{-1}) for 15 min. The supernatant liquid was collected after centrifugation (10 min, 7500 rpm) and used for steady-state emission and fs-transient absorption spectroscopy.

Steady-state emission spectra (λ_{ex} = 380 nm) were recorded with a FLS980 spectrometer (Edinburgh Instruments) in a 1 cm quartz cell. Time resolved emission data were recorded using a Hamamatsu HPDTA streak camera. A Ti:sapphire laser (Tsunami, Newport Spectra-Physics GmbH) was used as the light source and a pulse selector (model 3980, Newport Spectra-Physics GmbH) was used to reduce the repetition rate of the pulse train to 400 kHz. The emission was collected from a 1 cm cuvette in a 90° angle between the pump beam and a CHROMEX spectrograph detector. Analysis of the time-resolved emission data was performed using DecayFit software. Femtosecond (fs) transient absorption spectra were collected by using a previously reported home-built pump-probe laser system[31] based on an amplified Ti:sapphire oscillator (Libra, Coherent Inc.). The pump pulses centered at 325 nm were generated in a collinear optical-parametric amplifier (TOPAS-C, LightConversion Ltd.). The power of the pump beam was kept at 0.15 mW before samples. The white light continuum between 450 and 785 nm used to probe the photoexcited sample is generated by focusing a part of the fundamental laser output into an eccentrically rotating CaF_2 plate. The resultant supercontinuum is delayed in time with respect to the pump beam by means of an optical delay line and the polarization between probe and pump is set at the magic angle. The data were collected from the suspensions in 1 cm cuvettes.

Photopotential measurements. 50 mg of photocatalyst were suspended in 250 μL of methanol and sonicated for 5 minutes. Then, 200 μL of the suspension was smeared onto an FTO glass by doctor blading using a scotch tape as frame and spacer. The photoelectrodes were dried at 100 °C for 15 minutes and pressed for 3 minutes at a pressure of 200 kg cm^{-2}. The photoelectrochemical setup consisted of a SP-300 BioLogic potentiostat and a three-electrode configuration using a platinum counter electrode and a Ag/AgCl (3 M KCl) reference electrode. The photoelectrodes were pressed against an O-ring of the cell leaving an irradiated area of 0.5 cm^2. The measurements were collected under open circuit voltage conditions. The photoelectrodes were irradiated from the backside (through the FTO glass) by monochromatic light of 380 nm (Instytut Fotonowy). The measurements were conducted in a pH 7 lithium perchlorate electrolyte under argon atmosphere (solution was bubbled with Ar for 30 minutes) in the absence of any sacrificial electron donor.

2.4 Photocatalytic studies

The preliminary photocatalytic experiments showed that the nominal mass ratio of 1 : 10 ($\{Mo_3\}$: CN_x) was optimal for photocatalytic activity (see ESI, Fig. S1†), hence the detailed study of the photocatalytic properties was focused on this material in the following. The photocatalytic hydrogen evolution experiments were carried out using a custom-built air-cooling apparatus for maintaining room temperature (22 °C) and constant irradiation of the sample. Experiments were carried out in 21 mL Schlenk tubes capped with rubber septa. 10 mg of the CN_x-based catalysts were added to the Schlenk tube equipped with magnetic stirrer. The tube was evacuated and filled with argon. A H_2O : MeOH (9 : 1, v/v) solution, with or without addition of additional sacrificial electron donor, was purged with argon. 10 mL of the degassed solution were added to the photocatalyst in the Schlenk tube under inert conditions and kept under constant irradiation from a LED source (λ = 420 nm; *ca.* 50 mW cm^{-2}) in air-cooled photoreactors. The gas phase of the Schlenk tube was probed by inserting a gas-tight GC syringe through the septum and the amount of hydrogen in the gas phase was quantified using headspace gas chromatography.

Gas chromatography. Gas-chromatography (GC) was performed on a Bruker Scion GC/MS, with a thermal conductivity detector 15 (column: molecular sieve 5A 75 m × 0.53 mm, oven temperature 70 °C, flow rate 25 mL min^{-1}, detector temperature 200 °C) with Argon as carrier gas. The GC was calibrated by direct injection of known amounts of H_2 gas.

3. Results and discussion

X. Wang *et al.* demonstrated that the interaction between the negatively charged $[Mo_3S_{13}]^{2-}$ [=$\{Mo_3\}$] clusters and the polymeric carbon nitride surface can be reinforced by protonation of the latter, thus providing stronger electrostatic interaction.[26] However, it was shown that $\{Mo_3\}$ is also efficiently immobilized on negatively charged carbon surfaces, bearing –OH and

–COOH functional groups.[17] Polymeric carbon nitride (PCN), apart from its polyheptazine structure, also possesses various functional amino-groups that have positive charges and can play an important role as anchoring sites *via* electrostatic interactions and hydrogen bonding.[32,33] One can therefore expect that $\{Mo_3\}$ would selectively attach to these surface moieties without covering the entire polymeric carbon nitride surface. According to ICP data, the actual loadings of the $Na_2[Mo_3S_{13}]\cdot 5H_2O$ clusters in the CN_x samples are 0.24, 0.85 and 2.06 wt% for the nominal loadings of 2, 10 and 20 wt%, respectively. The deposition of the $\{Mo_3\}$ clusters onto carbon nitride does not affect the support's long-range order as only a slight reduction of the intensity of the characteristic (100) and (002) maxima is observed in the composite's XRD pattern with respect to the pristine CN_x, which is, most likely, related to its partial exfoliation under sonication (Fig. 1a). FTIR spectra corroborate the absence of significant structural changes in CN_x caused by the co-catalyst incorporation (Fig. 1b; see also a detailed discussion in ESI†). However, we note the reduction of the relative intensity of the peak around 3125 cm^{-1} in the spectrum of CN_x–$\{Mo_3\}$ (Fig. 1b). This can be assigned either to partial elimination of the uncondensed NH_x-groups caused by ultrasonication treatment or to their interaction with the $\{Mo_3\}$ clusters. Only a small fraction of the $[Mo_3S_{13}]^{2-}$ species present in the initial solution is retained on the CN_x surface after washing. XPS surface elemental analysis of the CN_x–$\{Mo_3\}$ sample (10 wt% loading) allows to estimate that the Mo : N atomic ratio in the sample is only about 0.03, which implies that there is approximately one $\{Mo_3\}$ cluster for every 13 heptazine units. XPS analysis confirms that the polymeric carbon nitride structure has not suffered significant structural changes upon $\{Mo_3\}$ deposition. The C 1s spectrum displays two peaks located at 288.3 eV and 284.8 eV (ESI, Fig. S2†). The peak with binding energy of 288.3 eV is assigned to the typical aromatic C–N=C species in the triazine rings of the CN_x framework and the peak at 284.8 eV can be attributed to adventitious carbon (Fig. S2†). In the N 1 s spectra of the composite three peaks located at 398.7, 399.6 and 401.1 eV can be ascribed to the C–N=C, N–C_3 and C–NH_x groups, respectively (Fig. S2†).[33] As to the anchored $\{Mo_3\}$, the presence of Mo in the hybrid becomes evident by analysis of the spectra in the Mo 3d range. Apart of the S 2 s peak at 226.7 eV, which also appears in this energy range, two Mo 3d peak doublets are detected. The first one with dominating intensity at 229.1 and 232.2 eV can be attributed to Mo^{4+} and is most probably related to the $\{Mo_3\}$ particles (Fig. 1c).[34] The second doublet at 232.2 and 235.3 eV is most likely due to traces of Mo^{6+} formed upon partial exchange of S_2^{2-} by hydroxide or water ligands. The S 2p spectrum is more informative, since it confirms the integrity of the immobilized $\{Mo_3\}$ clusters. The S 2p spectrum can be fitted by introducing two doublet peaks ($2p_{3/2}$ and $2p_{1/2}$). The doublet at (161.9 eV and 163.1 eV) is attributed to the terminal S_2^{2-} ligands and the doublet at

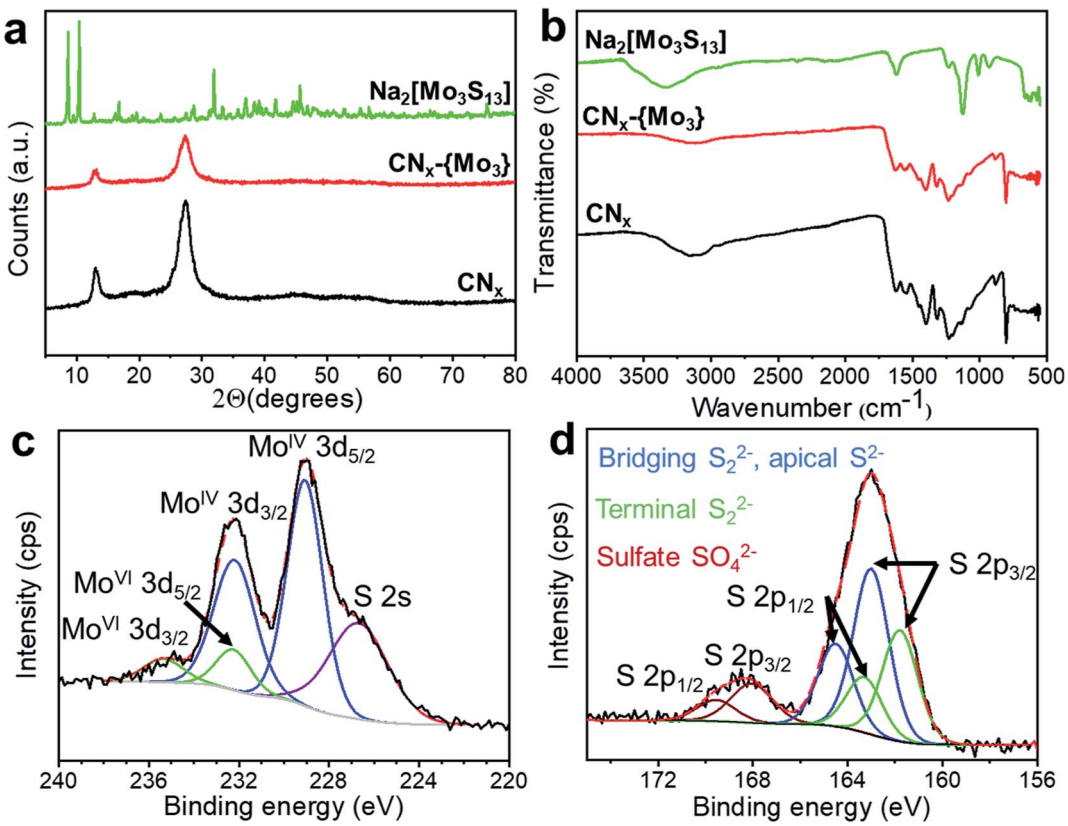

Fig. 1 Characterization of materials: (a) XRD patterns; (b) FTIR spectra. Deconvoluted XP spectra in the Mo 3d (c) and S 2p (d) range of CN_x–$\{Mo_3\}$ (10 wt% loading) photocatalyst.

(163.1 eV and 164.3 eV) is assigned to the apical S^{2-} and bridging S_2^{2-} in the $[Mo_3S_{13}]^{2-}$ clusters (Fig. 1d).[17,34] Finally, the presence of sulfate species in the composite is indicated by another peak doublet at higher binding energy (168.1 and 169.3 eV), characteristic for S–O binding. We assume that the sulfate was generated during the cation exchange process from residual sulfur existing in $(NH_4)_2Mo_3S_{13}\cdot 2H_2O$ (Fig. 1d).

Fig. 2 shows the results of the TEM investigation of CN_x–$\{Mo_3\}$. The overview images depict mostly large pieces of amorphous and undefined structure (Fig. 2a), however, crystalline flakes are also detectable in TEM (Fig. 2b). Energy filtered TEM images show a homogeneous distribution of Mo on the surface of the CN_x material (Fig. 2a). It should be mentioned that the crystalline flakes were amorphized as result of electron irradiation when acquiring elemental maps (Fig. 2c). The diffraction pattern and FFT (fast Fourier transform) of the crystalline flakes show first order reflection at 2.2 nm^{-1}, which can be attributed to a polymeric carbon nitride phase (Fig. 2b insets). Elemental mapping performed on the amorphous and crystalline parts of the sample shows uniform distribution of the $\{Mo_3\}$ clusters in CN_x material. We note that $\{Mo_3\}$ deposition leads to a reduction of the specific surface area from 13 down to 5 $m^2\ g^{-1}$.

Another indirect indication of the homogeneous distribution of the $\{Mo_3\}$ clusters within CN_x can be obtained from the TG data (Fig. 3a, ESI Fig. S3†). The decomposition onset is shifted by *ca.* 100 °C towards the low-temperature region for the CN_x–$\{Mo_3\}$ sample as compared to pristine CN_x (Fig. 3a). This increase of the thermal decomposition rate of the hybrid is due to the solid acid-catalyzed effect of the highly dispersed $\{Mo_3\}$ clusters or Mo oxides, which might be formed under thermal treatment in air. A similar effect was also reported for other metal oxide-doped polymeric carbon nitride systems.[35]

The optical absorption edge of CN_x remains the same after the incorporation of the $\{Mo_3\}$ clusters (Fig. 3b); the only additional feature is a broad absorption tail in the visible region that can be attributed to electronic transitions within finely distributed $\{Mo_3\}$ clusters.

3.1 Light-driven hydrogen evolution

The importance of ultrasonication during the depostition of co-catalyst is illustrated by the increased activity of the ultrasonicated materials in photocatalytic HER (ESI, Fig. S4†). Henceforth, this procedure was applied to all photocatalysts discussed below. Preliminary experiments were performed to establish the optimal conditions for carrying out photocatalytic HER reactions in suspensions of the prepared materials. These initial investigations showed that optimum $\{Mo_3\}$ cluster loading onto CN_x was 10 wt% (ESI, Fig. S1†), and subsequently other conditions were optimized for the CN_x–$\{Mo_3\}$ sample

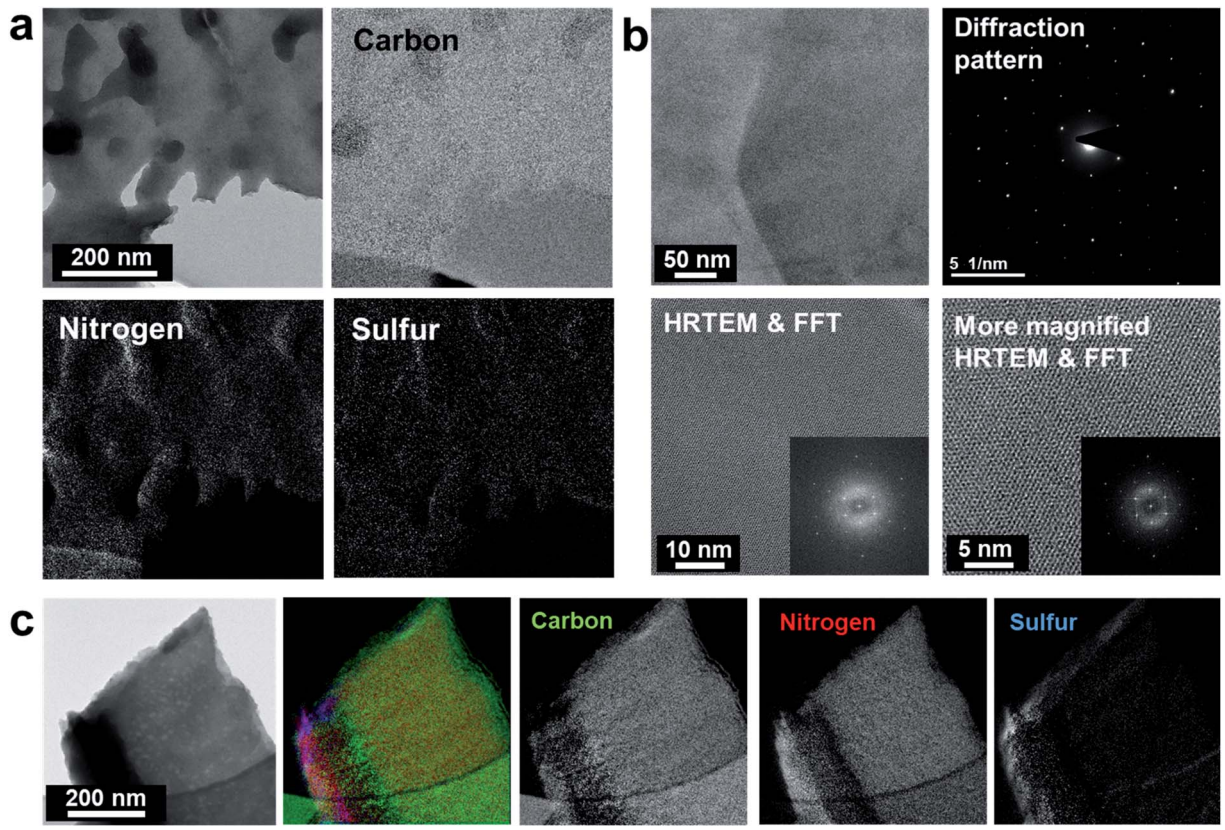

Fig. 2 TEM analysis of the amorphous crystalline areas of the CN_x–$\{Mo_3\}$ (10 wt% loading) sample. (a) Bright-field image of the amorphous area and corresponding energy filtered images showing the distribution of carbon, nitrogen and sulfur. (b) Overview image, diffraction pattern and HRTEM images with corresponding local FFT patterns of a crystalline area of the sample. (c) Large overview image and corresponding elemental distributions of a crystalline flake of the sample.

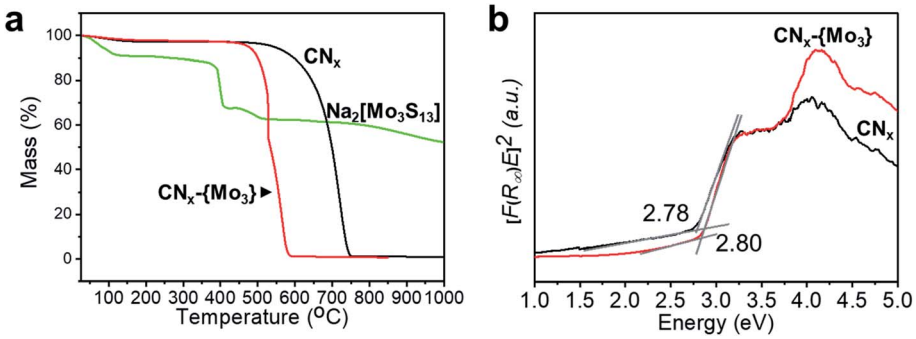

Fig. 3 (a) Thermogravimetric analysis of the prepared materials in air and (b) Tauc-plots of the studied CN_x photocatalysts with and without $\{Mo_3\}$ clusters (10 wt% loading).

permitting it to attain its highest activity using 10 mg of the photocatalyst in 10 mL of a H_2O : MeOH (9 : 1, v/v) solution with near neutral pH. The presence of 10% MeOH in the reaction medium, apart from playing a role of sacrificial reducing agent, also inhibits ligand-exchange reaction of the $\{Mo_3\}$ cluster, where surface S_2^{2-} might be gradually exchanged with hydroxide or water ligands.[28] The pristine carbon nitride sample (CN_x) does not show any significant H_2 evolution activity under given conditions (Fig. 4a), while the CN_x–$\{Mo_3\}$ is clearly active in this reaction. Few points are noteworthy in this context. Firstly, $\{Mo_3\}$ clusters trigger the photocatalytic H_2 evolution even in the presence of methanol, a much weaker reducing agent than lactic acid used by Wang *et al.*[26] The rate of H_2 evolution was stable over 24 hours (ESI, Fig. S5a†), and the external quantum efficiency (EQE) of H_2 evolution at 420 nm in the presence of methanol was estimated as 0.055% and 0.19% for CN_x modified with $\{Mo_3\}$ and Pt, respectively. Not surprisingly, the activity towards H_2 evolution can be enhanced by the application of additional electron donor such as ascorbic acid (ESI, Fig. S5b† and 4b). Furthermore, though the activity of CN_x–$\{Mo_3\}$ is well below that of the benchmark Pt-CN_x (Fig. 4a and S5a†), we note that platinum is more expensive than molybdenum by the factor of ~1000, which eventually might become a determining factor for the development of such systems. Interestingly, addition of an alternative widely used sacrificial reducing agent, triethanolamine (TEOA), lowered the yield of H_2 (Fig. 4b), which can be explained by the decomposition of $\{Mo_3\}$ clusters in the highly basic solution of TEOA.

3.2 Optical spectroscopy of CN_x–$\{Mo_3\}$

To investigate the excitonic processes involved in the system, we performed steady-state photoluminescence (PL), time-resolved PL and fs-transient absorption (fs-TA) measurements. Fig. 5a and b depict the photoluminescence properties of pristine CN_x and CN_x–$\{Mo_3\}$ upon 380 nm excitation. All samples show identical photoluminescence spectra peaking at 440 nm corresponding to optical bandgap emission. Compared to pristine CN_x, addition of $\{Mo_3\}$ at the loading of 10 wt% and 20 wt% quenches the emission, which indicates an enhanced separation efficiency of the photoinduced charge carriers at the interface of higher loading samples. However, at a very low loading (2 wt%), we observed an increase of the emission intensity. In order to explain this finding, we propose that the addition of few $\{Mo_3\}$ clusters leads to a situation in which the negatively charged clusters preferentially interact with the amine groups thereby breaking the amine hydrogen bonds with water or/and heptazine nitrogen atoms. The amine groups are apparently associated with shallow trapping states,[36,37] which upon addition of only 2 wt% $\{Mo_3\}$ shift in energy and can thermally repopulate emissive excitonic states. This is in line with the increase of the photoluminescence lifetime from 3.02 (pristine CN_x) to 5.49 ns (upon addition of 2 wt% $\{Mo_3\}$). The dropping photoluminescence intensity in 10 wt% CN_x–$\{Mo_3\}$ correlates with the shortened emission lifetime, which drops back to 3.18 ns. This indicates that the radiative rates of 2 wt% and 10 wt% CN_x–$\{Mo_3\}$ remain comparable. However, the

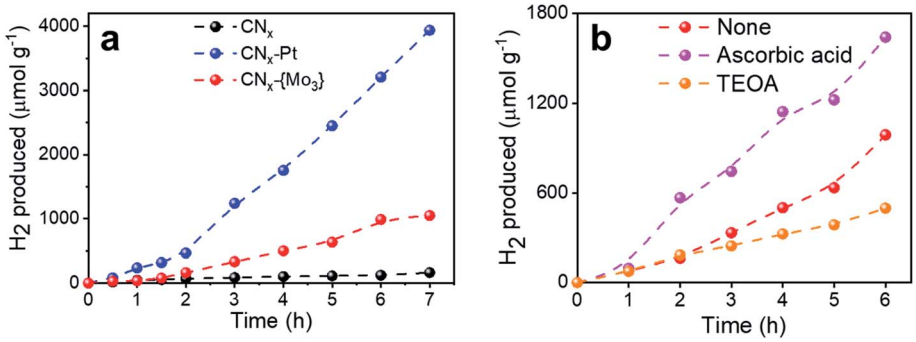

Fig. 4 Photocatalytic HER performed using CN_x based materials under 420 nm irradiation. Conditions: [catalyst]: 10 mg, solvent: 10 mL H_2O : MeOH (9 : 1, v/v), (a) in absence and (b) presence of additional electron donors [triethanolamine]: 10% or [ascorbic acid]: 0.1 M.

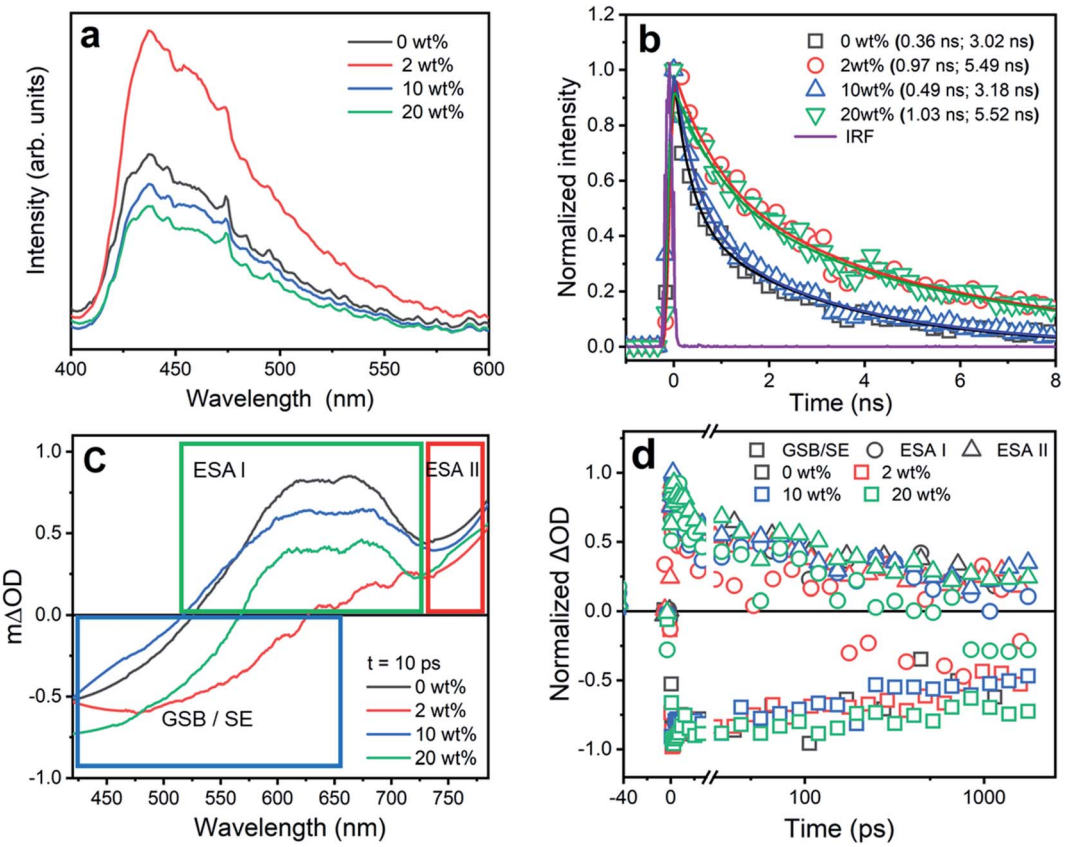

Fig. 5 (a) Steady-state photoluminescence spectra of CN_x suspensions at different loading ratios of $\{Mo_3\}$. The spectra were recorded upon excitation at 380 nm. (b) Time-resolved photoluminescence decay curves of $\{Mo_3\}$ functionalized CN_x suspensions (2 mg mL^{-1}) after 385 nm photoexcitation. The photoluminescence decay curves were generated by spectrally integrating streak camera data between 410 and 550 nm. (c) Transient absorption spectra taken upon excitation at 325 nm with a pump-probe delay of 10 ps. The spectra were smoothed by Savitzky–Golay method to reduce high-frequency noise from scattering; the original data are shown in the ESI (Fig. S6†). (d) fs-transient absorption decay kinetics of CN_x materials dispersed in H_2O upon 325 nm excitation. The pump pulses carried an energy of 0.3 μJ per pulse. The transient absorption kinetics depicted were generated by spectrally integrating the transient absorption data in the probe wavelength ranges indicated in panel (c). GSB = ground state bleach; SE = stimulated emission; ESA = excited-state absorption.

addition of larger numbers of $\{Mo_3\}$ clusters leads to an increased non-radiative decay of the bandgap emission. The increased non-radiative decay is likely associated with the dissociation of band-edge or shallow trapped excitons into charge carriers at the CN_x–$\{Mo_3\}$ interface. To estimate the respective non-radiative rate associated with $\{Mo_3\}$-cluster induced charge carrier generation, $k_{nr}^{\{Mo_3\}}$, we assume that the non-radiative decay in 10 wt% CN_x–$\{Mo_3\}$ is an intrinsic non-radiative decay channel, which is also present in 2 wt% CN_x–$\{Mo_3\}$, *i.e.* $k_{nr}^{2wt\%}$. Under these assumptions one can consider $k_{nr}^{10wt\%} = k_{nr}^{2wt\%} + k_{nr}^{\{Mo_3\}}$. Based on the photoluminescence decay times and under the assumption that the radiative rates remain unchanged one yields $k_{nr}^{\{Mo_3\}} = 13.2 \times 10^7\ s^{-1}$, which can be considered the rate of cluster induced charge carrier generation from shallow trapped excitons in 10 wt% CN_x–$\{Mo_3\}$.

Upon increasing the loading to 20 wt% $\{Mo_3\}$, the lifetime of the emission increases again (to 5.52 ns) while the emission yield, as indirectly reflected in the photoluminescence intensity remains constant at best. Assuming that the non-radiative rates associated with charge generation are at least as high as in 10 wt% $\{Mo_3\}$, we have to conclude that the radiative rate drops upon increasing the cluster loading. This illustrates that high catalyst loading impacts the electronic structure of the underlying CN_x material causing the radiative rates to drop. It should be pointed out that the discussion laid out before is based on the two long lifetimes obtained from the bi-exponential fit of the photoluminescence decay. Fig. S8 in ESI† depicts the spectral components associated with the few-ns component and the sub-ns component. Considering the spectral characteristics of the components, we conclude that the blue-shifted short-lived photoluminescence stems from the band-edge emission, while the slower component reflects the decay of weakly trapped excitons.[38] In addition to the discussion above, we observe that the overall weight of the short-lived component to the time-resolved photoluminescence data decreases upon addition of $\{Mo_3\}$ clusters to the CN_x material. We associate this trend with an increased probability of bandgap exciton quenching by $\{Mo_3\}$ cluster-induced charge separation.

Next, we will consider fs transient absorption data recorded for the differently loaded CN_x materials upon excitation at 325 nm. Given the specific experimental setup, the data are recorded up to delay times of 1.8 ns. The transient absorption

spectra recorded at a pump-probe delay of 10 ps (see Fig. 5c) show a region of negative feature, which contains contributions from ground state bleach (GSB) and stimulated emission (SE) and two excited-state absorption (ESA) features, one at roughly 650 nm and one peaking towards the near-IR. The contribution from SE is apparent when comparing the shape of the negative transient absorption feature: for 2 wt% $\{Mo_3\}$, the sample with the highest emission intensity, the negative band extends furthest to the red and partially overlaps with the visible ESA band (which we refer to as ESA I).

To compare the photoinduced kinetics for the different materials, the characteristic transient absorption signals, *i.e.* GSB, the ESA in the visible and near-IR regions (Fig. 5c), are spectrally integrated in the respective wavelength ranges. The resultant kinetics are normalized and depicted in Fig. 5d. It is apparent that the addition of the $\{Mo_3\}$ catalysts does not impact the ultrafast photoinduced kinetics in the CN_x materials. Similar results are also observed for CN_x samples loaded with Pt-nanoparticles as a catalyst (see Fig. S7†), where the time resolved PL and transient absorption data do not show any significant changes compared to experiments done with CN_x alone. The data for the CN_x–Pt samples can also be understood in terms of an excited state decay following a power-law dependence and thus implying a trap-assisted recombination process.[39–41] This is reminiscent of the results obtained for polymeric carbon nitride modified with Pt *via* photodeposition.[41]

3.3 Photopotential transient measurements

While the fs transient absorption data indicate ultrafast photoinduced kinetics (on ps timescale), which are not notably affected by the molecular $\{Mo_3\}$ catalyst, our photoluminescence quenching experiments revealed that the addition of larger amounts of $\{Mo_3\}$ catalyst is likely associated with the dissociation of the band-edge and/or shallow trapped excitons into charge carriers, *i.e.* to increased charge separation. Furthermore, we observed a significant effect of the catalyst on the photocatalytic turnover (Fig. 4). As the catalysis typically occurs on a rather slow time scale, we envisaged that the catalyst effects could be possibly followed by open-circuit photopotential transient measurements.[42–45] Indeed, this is the case as evidenced by the stark difference in photopotential transients recorded for CN_x powders (with and without catalysts) after deposition onto FTO glass (Fig. 6a). In such a system, the sign of the photopotential is determined by the competitive kinetics of electron and hole transfers at the FTO/CN_x and CN_x/

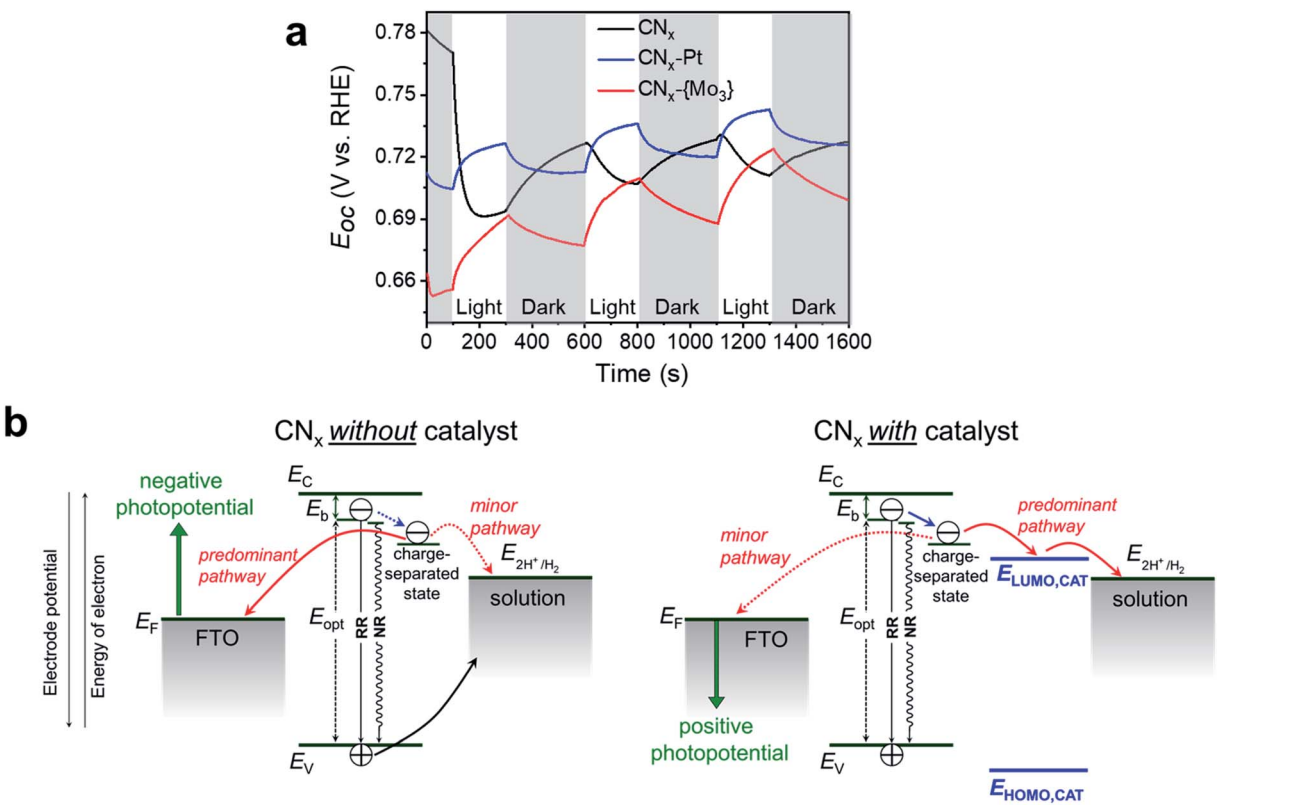

Fig. 6 (a) Open-circuit photopotential measurements of the CN_x, CN_x–Pt and CN_x–$\{Mo_3\}$ samples recorded in an aqueous $LiClO_4$ (0.1 M; pH 7) electrolyte (the solution was purged with argon prior to experiments); the materials were deposited on FTO and irradiated from the backside with monochromatic light ($\lambda = 380$ nm); (b) a simplified scheme showing the generation of photopotential at FTO/CN_x photoelectrodes without and with the $\{Mo_3\}$ catalyst: E_c and E_v stand for the conduction and valence band edge of CN_x; RR and NR stand for radiative and non-radiative recombination from emissive (band-edge) and non-emissive (shallow-trap) excitonic states, respectively; other recombination pathways are omitted for the sake of clarity; E_{opt} designates the optical bandgap of CN_x, E_b stands for the exciton binding energy and was estimated as ~0.3 eV according to ref. 47, the HOMO–LUMO gap of the catalyst has been estimated as 2.5 eV by DFT calculations (see the ESI for details†).

(catalyst)/solution interfaces. The very small values of the photopotentials, as compared to conventional semiconductors, are related to the strongly insulating character of polymeric CN_x,[46] and to the rather low quality of electric contact between CN_x and FTO. Notably, pristine CN_x without any catalyst exhibits small *negative* photopotentials, meaning that the photogenerated electrons do not readily react with the electrolyte, but are instead accumulated in CN_x and in the underlying FTO substrate. In contrast, after introducing the catalysts, either Pt or $\{Mo_3\}$, the photopotential behaviour is completely reversed and the photopotentials are *positive* now. This shows that, in the presence of the catalyst, the photogenerated electrons are more effectively extracted by the catalyst – as already corroborated by the observed decrease of the photoluminescence intensity and increase of the non-radiative decay into the charge separated state – and react faster with protons in solution, while the oxidizing equivalents (holes) are accumulated in CN_x and shift the Fermi level of the FTO to more positive potentials (Fig. 6b). This experiment clearly confirms, in analogy to conventional Pt hydrogen evolution catalyst,[47] the strong effect of molecular $\{Mo_3\}$ clusters on exciton dissociation and the catalyzed transfer of trapped electrons from CN_x to protons in the solution.

Conclusions

The electron accumulation in polymeric carbon nitride photocatalysts is known to be one of the major bottlenecks in light-driven hydrogen evolution,[48,49] and has been typically addressed by deposition of Pt,[49–51] Ni-based molecular catalysts,[52–54] or enzymes.[11,55] We investigated polymeric carbon nitride coupled with thiomolybdate $\{Mo_3\}$ clusters as an inexpensive alternative to widespread Pt-containing systems. The $\{Mo_3\}$ clusters do promote the hydrogen evolution reaction under visible light irradiation in the presence of methanol or other (stronger) reducing agents, yet the activity of CN_x–$\{Mo_3\}$ composites was found to be significantly lower than that of CN_x–Pt benchmark photocatalysts. While the deposition of the $\{Mo_3\}$ clusters does not induce any significant structural alteration of the polymeric carbon nitride absorber, the loading of the $\{Mo_3\}$ catalyst exerts an influence on exciton and charge transfer dynamics. At sub-optimal (low) $\{Mo_3\}$ cluster loadings the excitons are trapped in shallow states within a few ns. These non-emissive excitonic states (shallow traps) are apparently in a thermal equilibrium with band-edge emissive states leading to enhanced photoluminescence. At higher $\{Mo_3\}$ catalyst loading, the transient PL measurements show that the excitons dissociate more effectively, forming thus more populated charge-separated (deep trap) states. This is followed by more efficient electron transfer to the catalyst and protons in the solution, as indicated by the change of the sign of the open-circuit photopotential to positive (Fig. 6b). Finally, three points are noteworthy. First, the charge transfer to the catalyst, both molecular $\{Mo_3\}$ clusters and Pt nanoparticles, definitely occurs on a relatively longer (ns to s) time scale, as neither $\{Mo_3\}$ nor Pt catalysts had impact on the ultrafast (sub-ns) photoinduced kinetics in the CN_x materials. These results are consistent with recent reports by Durrant *et al.*,[48] suggesting that generation of "long-lived" (>ns time scale) electrons is beneficial for enhancing the photoactivity in hydrogen evolution. Second, while the charge-separated deep trap states play an important role in the CN_x–$\{Mo_3\}$ system by facilitating the exciton dissociation, it cannot be ruled out that they also act as recombination centers, which – in view of further improvements on photocatalytic activity of carbon nitrides – makes an elaborated engineering of their electronic and interfacial properties mandatory. Third, as the emissive decay kinetics shows an obvious deviation from pristine CN_x at non-optimal catalyst loadings (2 and 20 wt%) but not in case of the optimal loading (10 wt%), the design and development of appropriate synthetic strategies for optimizing the catalyst loading without affecting negatively the electronic structure of the CN_x materials is essential for enhancing the photoconversion efficiencies.

Author contributions

T. J., C. S., B. D., D. M. and R. B. conceived the research and lead the project. A. R., E. A., D. M., C. A. and I. K. performed the synthesis and characterization of materials, interpreted all data, and wrote the manuscript. J. B. and U. K. performed the TEM measurements and analysis. T. D. performed the XPS analysis. C. L. and B. D. performed the spectroscopy studies. C. I. and T. J. performed theoretical calculations. All authors wrote and commented on the manuscript.

Conflicts of interest

The authors declare no competing interests.

Acknowledgements

This work was funded by the Deutsche Forschungsgemeinschaft (DFG, German Research Foundation) – Projektnummer 364549901 – TRR 234 CataLight [Projects A5, B6, and C4]. Computational resources were provided by the state of Baden-Württemberg through bwHPC and the DFG (INST 40/467-1 FUGG). I. K. acknowledges the support of the Alexander von Humboldt Foundation through the Humboldt Research Fellowship. Dr Carola Hoffmann-Richter and Margit Lang are acknowledged for TGA and ICP-AES measurments, respectively. We are grateful to Alexander Schleusener for assistance performing initial time-resolved spectroscopic experiments.

References

1 J. Barber, *Sustainable Energy Fuels*, 2018, **2**, 927–935.
2 A. Kudo and Y. Miseki, *Chem. Soc. Rev.*, 2009, **38**, 253–278.
3 X. Chen, S. Shen, L. Guo and S. S. Mao, *Chem. Rev.*, 2010, **110**, 6503–6570.
4 G. Zhang, Z.-A. Lan and X. Wang, *Angew. Chem., Int. Ed.*, 2016, **55**, 15712–15727.
5 M. F. Kuehnel and E. Reisner, *Angew. Chem., Int. Ed.*, 2018, **57**, 3290–3296.

6 X. Zou and Y. Zhang, *Chem. Soc. Rev.*, 2015, **44**, 5148–5180.
7 X. Wang, K. Maeda, A. Thomas, K. Takanabe, G. Xin, J. M. Carlsson, K. Domen and M. Antonietti, *Nat. Mater.*, 2009, **8**, 76–80.
8 X. Wang, K. Maeda, X. Chen, K. Takanabe, K. Domen, Y. Hou, X. Fu and M. Antonietti, *J. Am. Chem. Soc.*, 2009, **131**, 1680–1681.
9 N. Wang, J. Wang, J. Hu, X. Lu, J. Sun, F. Shi, Z.-H. Liu, Z. Lei and R. Jiang, *ACS Appl. Energy Mater.*, 2018, **1**, 2866–2873.
10 K. Maeda, X. Wang, Y. Nishihara, D. Lu, M. Antonietti and K. Domen, *J. Phys. Chem. C*, 2009, **113**, 4940–4947.
11 C. A. Caputo, M. A. Gross, V. W. Lau, C. Cavazza, B. V. Lotsch and E. Reisner, *Angew. Chem., Int. Ed.*, 2014, **53**, 11538–11542.
12 J. Wang, J. Chen, P. Wang, J. Hou, C. Wang and Y. Ao, *Appl. Catal., B*, 2018, **239**, 578–585.
13 X. Lu, J. Xie, S.-y. Liu, A. Adamski, X. Chen and X. Li, *ACS Sustainable Chem. Eng.*, 2018, **6**, 13140–13150.
14 Y. Wu, H. Wang, W. Tu, S. Wu, Y. Liu, Y. Z. Tan, H. Luo, X. Yuan and J. W. Chew, *Appl. Catal., B*, 2018, **229**, 181–191.
15 Y. Hou, Y. Zhu, Y. Xu and X. Wang, *Appl. Catal., B*, 2014, **156–157**, 122–127.
16 L. Ge, C. Han, X. Xiao and L. Guo, *Int. J. Hydrogen Energy*, 2013, **38**, 6960–6969.
17 J. Kibsgaard, T. F. Jaramillo and F. Besenbacher, *Nat. Chem.*, 2014, **6**, 248–253.
18 H. I. Karunadasa, E. Montalvo, Y. Sun, M. Majda, J. R. Long and C. J. Chang, *Science*, 2012, **335**, 698–702.
19 T. F. Jaramillo, K. P. Jørgensen, J. Bonde, J. H. Nielsen, S. Horch and I. Chorkendorff, *Science*, 2007, **317**, 100–102.
20 K. Du, L. Zheng, T. Wang, J. Zhuo, Z. Zhu, Y. Shao and M. Li, *ACS Appl. Mater. Interfaces*, 2017, **9**, 18675–18681.
21 Y. Shang, X. Xu, B. Gao and Z. Ren, *ACS Sustainable Chem. Eng.*, 2017, **5**, 8908–8917.
22 Y. Shang, X. Xu, Z. Wang, B. Jin, R. Wang, Z. Ren, B. Gao and Q. Yue, *ACS Sustainable Chem. Eng.*, 2018, **6**, 6920–6931.
23 M.-L. Grutza, A. Rajagopal, C. Streb and P. Kurz, *Sustainable Energy Fuels*, 2018, **2**, 1893–1904.
24 D. Recatalá, R. Llusar, A. L. Gushchin, E. A. Kozlova, Y. A. Laricheva, P. A. Abramov, M. N. Sokolov, R. Gómez and T. Lana-Villarreal, *ChemSusChem*, 2015, **8**, 1299.
25 I. Romanenko, A. Rajagopal, C. Neumann, A. Turchanin, C. Streb and F. H. Schacher, *J. Mater. Chem. A*, 2020, **8**, 6238–6244.
26 F. Guo, Y. Hou, A. M. Asiri and X. Wang, *Chem. Commun.*, 2017, **53**, 13221–13224.
27 A. Rajagopal, F. Venter, T. Jacob, L. Petermann, S. Rau, S. Tschierlei and C. Streb, *Sustainable Energy Fuels*, 2019, **3**, 92–95.
28 M. Dave, A. Rajagopal, M. Damm-Ruttensperger, B. Schwarz, F. Nägele, L. Daccache, D. Fantauzzi, T. Jacob and C. Streb, *Sustainable Energy Fuels*, 2018, **2**, 1020–1026.
29 Y. Han, D. Yue, M. Kan, Y. Wu, J. Zeng, Z. Bian, Y. Zhao and X. Qian, *Appl. Catal., B*, 2019, **245**, 190–196.
30 A. Müller, V. Wittneben, E. Krickemeyer, H. Bögge and M. Lemke, *Z. Anorg. Allg. Chem.*, 1991, **605**, 175–188.
31 R. Siebert, D. Akimov, M. Schmitt, A. Winter, U. S. Schubert, B. Dietzek and J. Popp, *ChemPhysChem*, 2009, **10**, 910–919.
32 M. Ilkaeva, I. Krivtsov, E. Bartashevich, S. Khainakov, J. Garcia, E. Diaz and S. Ordonez, *Green Chem.*, 2017, **19**, 4299–4304.
33 I. Krivtsov, D. Mitoraj, C. Adler, M. Ilkaeva, M. Sardo, L. Mafra, C. Neumann, A. Turchanin, C. Li, B. Dietzek, R. Leiter, J. Biskupek, U. Kaiser, C. Im, B. Kirchhoff, T. Jacob and R. Beranek, *Angew. Chem., Int. Ed.*, 2020, **59**, 487–495.
34 C.-H. Lee, S. Lee, Y.-K. Lee, Y. C. Jung, Y.-I. Ko, D. C. Lee and H.-I. Joh, *ACS Catal.*, 2018, **8**, 5221–5227.
35 Y. He, J. Cai, T. Li, Y. Wu, Y. Yi, M. Luo and L. Zhao, *Ind. Eng. Chem. Res.*, 2012, **51**, 14729–14737.
36 Y. Kang, Y. Yang, L.-C. Yin, X. Kang, L. Wang, G. Liu and H.-M. Cheng, *Adv. Mater.*, 2016, **28**, 6471–6477.
37 X. Li, I. V. Sergeyev, F. Aussenac, A. F. Masters, T. Maschmeyer and J. M. Hook, *Angew. Chem., Int. Ed.*, 2018, **57**, 6848–6852.
38 C. Merschjann, S. Tschierlei, T. Tyborski, K. Kailasam, S. Orthmann, D. Hollmann, T. Schedel-Niedrig, A. Thomas and S. Lochbrunner, *Adv. Mater.*, 2015, **27**, 7993–7999.
39 J. Nelson, *Phys. Rev. B: Condens. Matter Mater. Phys.*, 1999, **59**, 15374–15380.
40 J. J. Walsh, C. Jiang, J. Tang and A. J. Cowan, *Phys. Chem. Chem. Phys.*, 2016, **18**, 24825–24829.
41 R. Godin, Y. Wang, M. A. Zwijnenburg, J. Tang and J. R. Durrant, *J. Am. Chem. Soc.*, 2017, **139**, 5216–5224.
42 D. Monllor-Satoca and R. Gomez, *J. Phys. Chem. C*, 2008, **112**, 139–147.
43 S. Neubert, D. Mitoraj, S. A. Shevlin, P. Pulisova, M. Heimann, Y. Du, G. K. L. Goh, M. Pacia, K. Kruczala, S. Turner, W. Macyk, Z. X. Guo, R. K. Hocking and R. Beranek, *J. Mater. Chem. A*, 2016, **4**, 3127–3138.
44 S. Neubert, P. Pulisova, C. Wiktor, P. Weide, B. Mei, D. A. Guschin, R. A. Fischer, M. Muhler and R. Beranek, *Catal. Today*, 2014, **230**, 97–103.
45 C. Adler, D. Mitoraj, I. Krivtsov and R. Beranek, *J. Chem. Phys.*, 2020, **152**, 244702.
46 M. Bledowski, L. Wang, A. Ramakrishnan, O. V. Khavryuchenko, V. D. Khavryuchenko, P. C. Ricci, J. Strunk, T. Cremer, C. Kolbeck and R. Beranek, *Phys. Chem. Chem. Phys.*, 2011, **13**, 21511–21519.
47 S. Melissen, T. Le Bahers, S. N. Steinmann and P. Sautet, *J. Phys. Chem. C*, 2015, **119**, 25188–25196.
48 W. Yang, R. Godin, H. Kasap, B. Moss, Y. Dong, S. A. J. Hillman, L. Steier, E. Reisner and J. R. Durrant, *J. Am. Chem. Soc.*, 2019, **141**, 11219–11229.
49 V. W.-h. Lau, D. Klose, H. Kasap, F. Podjaski, M.-C. Pignié, E. Reisner, G. Jeschke and B. V. Lotsch, *Angew. Chem., Int. Ed.*, 2017, **56**, 510–514.
50 D. J. Martin, K. Qiu, S. A. Shevlin, A. D. Handoko, X. Chen, Z. Guo and J. Tang, *Angew. Chem., Int. Ed.*, 2014, **53**, 9240–9245.
51 D. J. Martin, P. J. T. Reardon, S. J. A. Moniz and J. Tang, *J. Am. Chem. Soc.*, 2014, **136**, 12568–12571.

52 T. Uekert, H. Kasap and E. Reisner, *J. Am. Chem. Soc.*, 2019, **141**, 15201–15210.
53 H. Kasap, R. Godin, C. Jeay-Bizot, D. S. Achilleos, X. Fang, J. R. Durrant and E. Reisner, *ACS Catal.*, 2018, **8**, 6914–6926.
54 H. Kasap, C. A. Caputo, B. C. M. Martindale, R. Godin, V. W.-h. Lau, B. V. Lotsch, J. R. Durrant and E. Reisner, *J. Am. Chem. Soc.*, 2016, **138**, 9183–9192.
55 C. A. Caputo, L. Wang, R. Beranek and E. Reisner, *Chem. Sci.*, 2015, **6**, 5690–5694.